SUPERMASSIVE POPULATION III SUPERNOVAE AND THE BIRTH OF THE FIRST QUASARS

Daniel J. Whalen[1], Alexander Heger[2], K.-J. Chen[3], Wesley Even[4], Chris L. Fryer[5], Massimo Stiavelli[6], Hao Xu[7] and Candace C. Joggerst[8]

Draft version November 9, 2012

ABSTRACT

The existence of supermassive black holes (SMBHs) as early as $z \sim 7$ is one of the great unsolved problems in cosmological structure formation. One leading theory argues that they are born during catastrophic baryon collapse in $z \sim 15$ protogalaxies in strong Lyman-Werner (LW) UV backgrounds. Atomic line cooling in such galaxies fragments baryons into massive clumps that are thought to directly collapse to 10^4 - 10^5 $M_\odot$ black holes. We have now discovered that some of these fragments can instead become supermassive stars that eventually explode as pair-instability supernovae (PI SNe) with energies of $\sim 10^{55}$ erg, the most energetic explosions in the universe. We have calculated light curves and spectra for supermassive Pop III PI SNe with the Los Alamos RAGE and SPECTRUM codes. We find that they will be visible in near infrared (NIR) all-sky surveys by *WFIRST* and *WISH* out to $z \sim 20$, perhaps revealing the birthplaces of the first quasars.

Subject headings: black hole physics - cosmology: early universe - theory - galaxies: formation – galaxies: high-redshift – stars: early-type – supernovae: general – radiative transfer – hydrodynamics – shocks

1. INTRODUCTION

One model for the origin of SMBHs, which have now been found at $z \sim 7$, or less than a Gyr after the big bang (Mortlock et al. 2011), is catastrophic baryon collapse in protogalaxies in strong LW UV backgrounds at $z \sim 15$ (Wise et al. 2008; Regan & Haehnelt 2009; Shang et al. 2010). In this scenario, the primitive galaxy is built up by mergers between halos and by accretion in the vicinity of nearby LW UV sources that completely suppress star formation in the halos without evaporating them (Wolcott-Green et al. 2011). When the galaxy reaches $\sim 10^8$ $M_\odot$, its virial temperature crosses the threshold for atomic hydrogen line emission and its baryons begin to rapidly cool and collapse. Infall rates at the center of the galaxy can be enormous: 0.1 - 1 $M_\odot$ yr^{-1}, or 1000 times those in which the first stars form at $z \sim 25$. Numerical simulations show that the baryons can shed angular momentum via the "bars within bars" instability on multiple spatial scales and collapse into an isothermal atomically-cooled disk. New simulations show that such disks can either feed a single massive central object or fragment into several slightly smaller ones (Regan & Haehnelt 2009; Whalen et al. 2012e). In Figure 1 we show the formation and fragmentation of such

[1] McWilliams Fellow, Department of Physics, Carnegie Mellon University, Pittsburgh, PA 15213
[2] Monash Centre for Astrophysics, Monash University, Victoria, 3800, Australia
[3] School of Physics and Astronomy, University of Minnesota, Twin Cities, Minneapolis, MN 55455
[4] XTD-6, Los Alamos National Laboratory, Los Alamos, NM 87545
[5] CCS-2, Los Alamos National Laboratory, Los Alamos, NM 87545
[6] Space Telescope Science Institute, 3700 San Martin Drive, Baltimore, MD 21218
[7] Center for Astrophysics and Space Sciences, UC San Diego, La Jolla, CA 92093
[8] XTD-3, Los Alamos National Laboratory, Los Alamos, NM 87545

a disk at the center of a 10^8 $M_\odot$ halo in a strong LW background at $z \sim 15$ in an adaptive mesh refinement (AMR) simulation done with Enzo[9].

The evolution of the fragments depends on their masses at birth and subsequent accretion histories (see Ohkubo et al. 2009, for studies of Pop III stellar evolution under ongoing accretion at much lower rates). One possibility is that a black hole forms at the center of the fragment early in the collapse that radiatively supports its surrounding envelope, a "quasistar" (Begelman et al. 2006, 2008; Begelman 2010; Volonteri & Begelman 2010). The fragment may instead gradually collapse while being partially supported by unstable nuclear burning, never reaching the main sequence or becoming a star. In this scenario, transient nuclear burning fails to offset gravity, and the fragment collapses to a 10^4 - 10^5 $M_\odot$ black hole (Fuller et al. 1986). If the clump has sufficient angular momentum, collapse proceeds via the formation of a black hole accretion disk system. If the fragment does form a star, recent calculations have shown that its UV radiation will probably not be able to halt accretion and it may evolve under heavy infall over its entire life (Johnson et al. 2012b). In contrast, lower-mass Pop III stars usually disperse the baryons from their halos (Whalen et al. 2004; Kitayama et al. 2004; Alvarez et al. 2006; Abel et al. 2007; Wise & Abel 2008). We note that other mechanisms for massive fragmentation and SMBH seed formation have been proposed, such as the suppression of gas cooling by primordial magnetic fields (Sethi et al. 2010) and cold accretion shocks (Inayoshi & Omukai 2012).

We have found that for a narrow range of mass around 55,000 $M_\odot$, atomically-cooled fragments can settle into stable nuclear burning and become supermassive stars with lifetimes of ~ 2 Myr. These stars die as extremely energetic PI SNe, with energies of
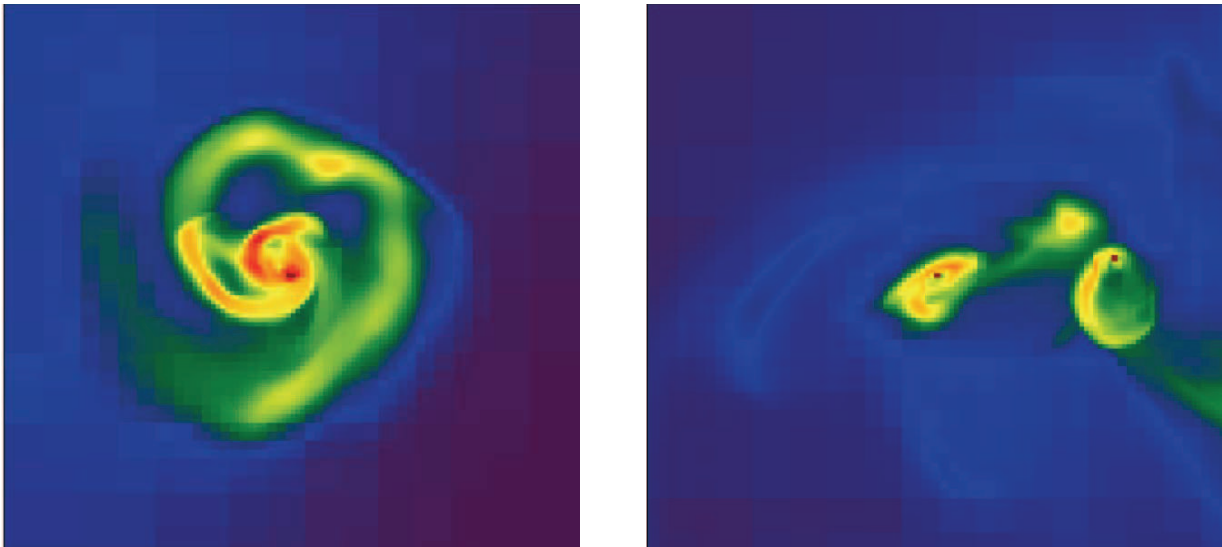
[9] http://code.google.com/p/enzo/

FIG. 1.— Baryon collapse at the center of a $z \sim 15$ protogalaxy in a LW UV background in the Enzo AMR code (Whalen et al. 2012e). Left: the formation of an atomically-cooled accretion disk at the center of the nascent galaxy at 10,000 yr. Right: the breakup of the disk into several supermassive fragments shortly thereafter. The scale is ~ 2000 AU.

$\sim 10^{55}$ erg, or 100 times those of 65 - 260 $M_\odot$ Pop III PI SNe (Rakavy & Shaviv 1967; Barkat et al. 1967; Heger & Woosley 2002; Gal-Yam et al. 2009). Such events would be the most energetic explosions in the universe, and their detection could reveal the birthplaces of SMBH created by direct collapse, since LW protogalaxies are the only environments known to form such massive fragments at $z \sim 15$. Could such SNe be discovered by existing or future observatories? Whalen et al. (2012c,b) recently found that 140 - 260 $M_\odot$ Pop III PI SNe will be detected in the NIR out to $z \gtrsim 30$ by the *James Webb Space Telescope* ((*JWST*) Gardner et al. 2006) and to $z \sim 15$ - 20 in all-sky surveys by the *Wide-Field Infrared Survey Telescope* (*WFIRST*) and the *Wide-Field Imaging Surveyor for High Redshift* (*WISH*). However, supermassive explosions might occur in extremely dense accretion envelopes that quench their luminosities at early times when the greatest fraction of their flux is redshifted into the NIR. It is not clear if SNe in such dense shrouds could be detected.

We present numerical simulations of light curves, spectra and NIR signals of supermassive Pop III PI SNe at $7 < z < 30$ done with the Los Alamos RAGE and SPECTRUM codes. We consider only the observational signatures of these events, and defer detailed discussion of progenitor evolution, explosive nucleosynthesis and multidimensional mixing to a forthcoming paper. In § 2 we review our numerical methods for evolving the star, its explosion, and the propagation of the blast through the star and its surrounding envelope. In § 3 we examine blast profiles, light curves and spectra for the SN in the source frame, and in § 4 we show NIR light curves in the observer frame and determine detection thresholds as a function of redshift for these explosions. In § 5 we conclude by discussing complementary detection strategies for the direct collapse of supermassive disk fragments and the formation of SMBH seeds.

2. NUMERICAL METHOD

We calculate light curves and spectra in three stages. First, we evolve the 55,500 $M_\odot$ zero metallicity star from the beginning of the main sequence through core collapse, nuclear burning, and the arrival of the shock at the edge of the star in the Kepler code. In a parallel calculation we map a Kepler profile of the star onto a 2D AMR grid in the CASTRO code at the onset of collapse and evolve it through core bounce, explosive burning and again up to just before shock breakout. Second, we spherically average mass fractions from the final CASTRO profile onto a 1D AMR grid in RAGE together with final density, velocity and energy profiles from the Kepler calculation. This is done to model how mixing in the interior of the star prior to shock breakout alters explosion spectra at later times. We evolve the shock through the surface of the star and into the surrounding medium with RAGE until it dims below observability. Finally, we post process our RAGE profiles with the SPECTRUM code to calculate light curves and spectra.

2.1. *Kepler*

We calculate the internal structure of the star by evolving it from the zero age main sequence to the beginning of collapse in the 1D stellar evolution code Kepler (Weaver et al. 1978; Woosley et al. 2002). The SN begins when the core of the star encounters the pair instability during central He burning, begins to contract, and triggers explosive O and Si burning (Heger & Woosley 2002; Scannapieco et al. 2005; Heger & Woosley 2010; Joggerst & Whalen 2011; Kasen et al. 2011; Pan et al. 2012a,b). The non-rotating star, which is resolved with 1148 mass zones, lives for 1.69 Myr and then dies as compact blue giant with a radius of 1.33×10^{13} cm, similar to those of the z-series stars in Whalen et al. (2012b) even though they are ~ 200 times more massive. The mass of the He core at the time of the explosion is 2.67×10^4 $M_\odot$. This treatment is approximate because the supermassive star would likely accrete gas throughout its life, and such flows will affect its evolution. If accretion onto the star is governed by radiative feedback (Johnson et al. 2012b), much of its evolution will proceed at a constant mass and our approach will be valid. The evolution of massive primordial clumps and supermassive stars under

ongoing accretion will be the focus of a future study.

2.2. *CASTRO*

At the beginning of core collapse we map our Kepler profiles onto a 2D axisymmetric grid in CASTRO (Almgren et al. 2010) and then evolve the SN through core bounce and explosive burning, halting the advance of the shock when it reaches the edge of the star in mass coordinate. CASTRO (Compressible ASTROphysics) is a multidimensional Eulerian AMR code with a unsplit Godunov hydrodynamics solver. Energy production is calculated with a 19-isotope network up to the point of oxygen depletion in the core and with a 128-isotope quasi-equilibrium network thereafter. We evolve mass fractions for the 15 even-numbered elements predominantly synthesized by PI SNe. Radiation transport is not required in these simulations because the mean free paths of photons prior to breakout are so short that they are simply advected through the star by the fluid flow. We include the contribution of photons to pressure in the equation of state. Our models include energy deposition due to radioactive decay of ^{56}Ni in the ejecta as described by equation 4 in Joggerst et al. (2010) although, as we discuss below, this explosion produces very little ^{56}Ni, unlike 140 - 260 $M_\odot$ Pop III PI SNe.

Mapping an explosion profile from a 1D Lagrangian coordinate mesh in mass to a 2D mesh in space can lead to violation of conservation of mass and energy. Linear interpolations in radius can also fail to resolve key features of the original profile, such as the structure of the core of the star and its temperature profile. Failure to properly map temperature features can be especially problematic because nuclear burn rates are highly sensitive to them during the explosion. To avoid these difficulties, we port Kepler profiles to CASTRO with the new conservative mapping scheme of Chen et al. (2011). This approach conserves mass and energy while reproducing all the features of the original profile over a broad dynamical range in space. The CASTRO root grid is 256^2 with a resolution of 2.0×10^{10} cm and up to two levels of AMR refinement (a factor of four increase in resolution).

The star explodes with an energy of 7.74×10^{54} erg. Explosive burning begins in the O and Si layers and is finished by ~ 100 s. The SN creates only trace amounts of ^{56}Ni, $\sim 2.25 \times 10^{-8}$ $M_\odot$, unlike 140 - 260 $M_\odot$ Pop III PI SNe that synthesize up to 50 $M_\odot$ of ^{56}Ni. The core of the SMS does not burn all the way to ^{56}Ni during the explosion as in less massive PI SNe. ^{56}Ni is only formed at the edge of the He layer by the shock as it is launched out into the star. As we show in Figure 2, the interior of the star is heavily mixed by the time the shock reaches the surface, unlike low-mass Pop III PI SNe that exhibit little mixing (Joggerst & Whalen 2011). The mixing is due to fluid instabilities that are seeded during core collapse and then amplified by explosive burning rather than the later formation of a reverse shock and the subsequent appearance of Rayleigh-Taylor instabilities, like those that mix the interiors of 15 - 40 $M_\odot$ Pop III core-collapse SNe (Joggerst et al. 2010). Pre-breakout mixing is important to explosion spectra because it determines the order in which emission and absorption lines appear in the spectra over time. Because elemental mass fractions are realistically distributed in radius and angle in CASTRO just

before shock breakout when we spherically average them and map them into RAGE, we can capture the approximate effect of mixing on spectral lines in 1D radiation hydrodynamical calculations. We stop the CASTRO run when the shock is no less than 100 photon mean free paths λ_p from the edge of the star:

$$\lambda_p = \frac{1}{\kappa_{\mathrm{Th}}\rho}, \qquad (1)$$

where κ_{Th} is the opacity due to Thomson scattering from electrons (0.288 gm^{-1} cm^2 for primordial gas), and ρ is the density just beyond the shock inside the star.

2.3. *RAGE*

We follow the shock through the surface of the star and its envelope with the Los Alamos National Laboratory (LANL) radiation hydrodynamics code RAGE (Gittings et al. 2008). RAGE (Radiation Adaptive Grid Eulerian) is a multidimensional AMR code that couples second order conservative Godunov hydrodynamics to grey or multigroup flux-limited diffusion (FLD) to model strongly radiating flows. RAGE utilizes the LANL OPLIB atomic opacity database[10] (Magee et al. 1995) and can evolve multimaterial flows with a variety of equations of state (EOS). We employ the same physics as in Frey et al. (2012): multispecies advection, grey FLD radiation transport with 2-temperature (2T) physics and LTE opacities, energy deposition from the radioactive decay of ^{56}Ni, and no self-gravity. Evolving radiation and matter temperatures separately in RAGE more accurately models shock breakout and its aftermath, when they can be out of equilibrium. We advect mass fractions for 15 elements, the even numbered elements predominantly synthesized by PI SNe.

We spherically average densities, velocities, specific internal energies (erg gm^{-1}), and species mass fractions from CASTRO onto a 50,000 zone 1D spherical AMR mesh in RAGE. Since radiation energy densities are not explicitly evolved in Kepler, we initialize them in RAGE as

$$E_{rad} = aT^4, \qquad (2)$$

where $a = 7.564 \times 10^{-15}$ erg cm^{-3} K^{-4} is the radiation constant and T is the gas temperature. Also, because the gas energy in Kepler includes contributions from the ionization states of atoms, we construct the specific internal energy from T with

$$E_{gas} = C_V T, \qquad (3)$$

where $C_V = 7.919 \times 10^7$ erg K^{-1} is the specific heat of the gas.

At the beginning of the simulation we resolve the region from the center of the grid to the edge of the shock in the velocity profile with 5000 zones on the root grid. We allow up to five levels of refinement during the initial mapping of the profile onto the grid and throughout the simulation. Our grid resolves all important density and velocity features in the setup with a minimum of 10 zones and up to 32 times more zones if needed. It

---

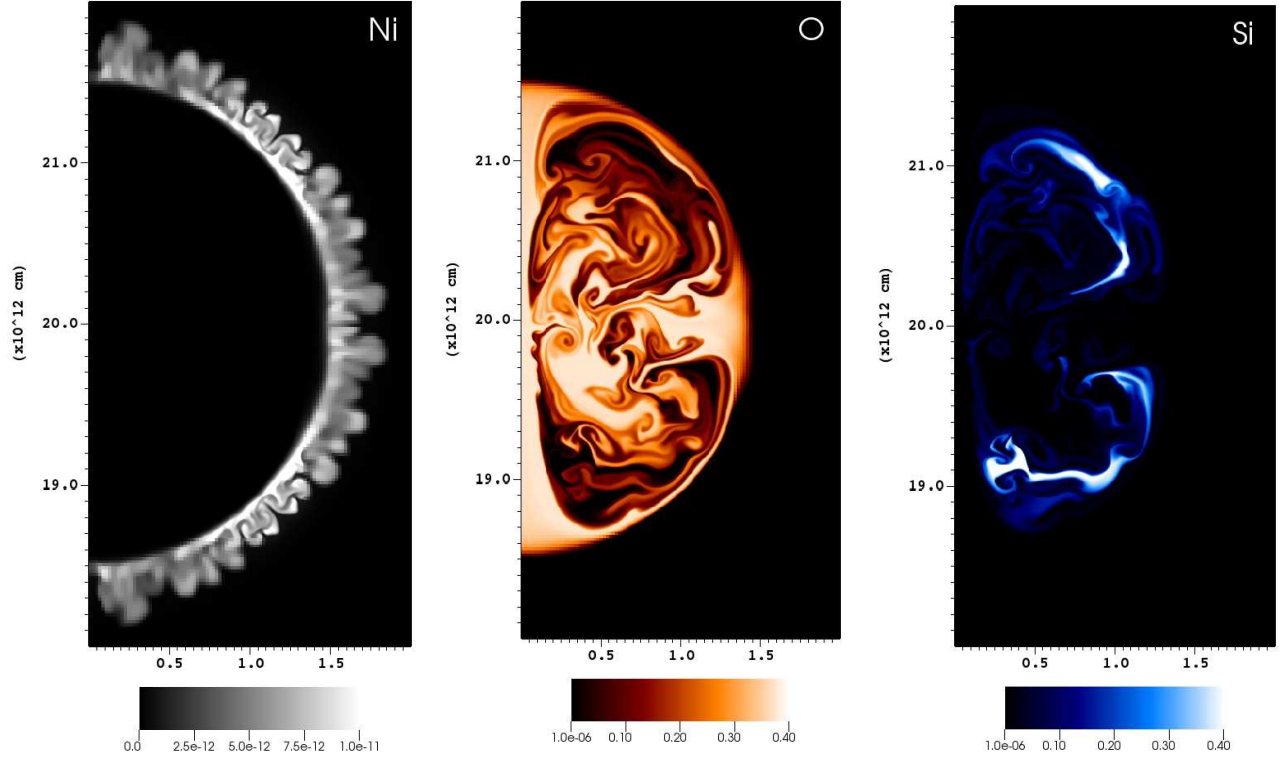[10] http://aphysics2/www.t4.lanl.gov/cgi-bin/opacity/tops.pl

FIG. 2.— Mixing in the Ni shell (left), O shell (center) and Si shell (right) just before shock breakout in CASTRO. The images are mass fractions.
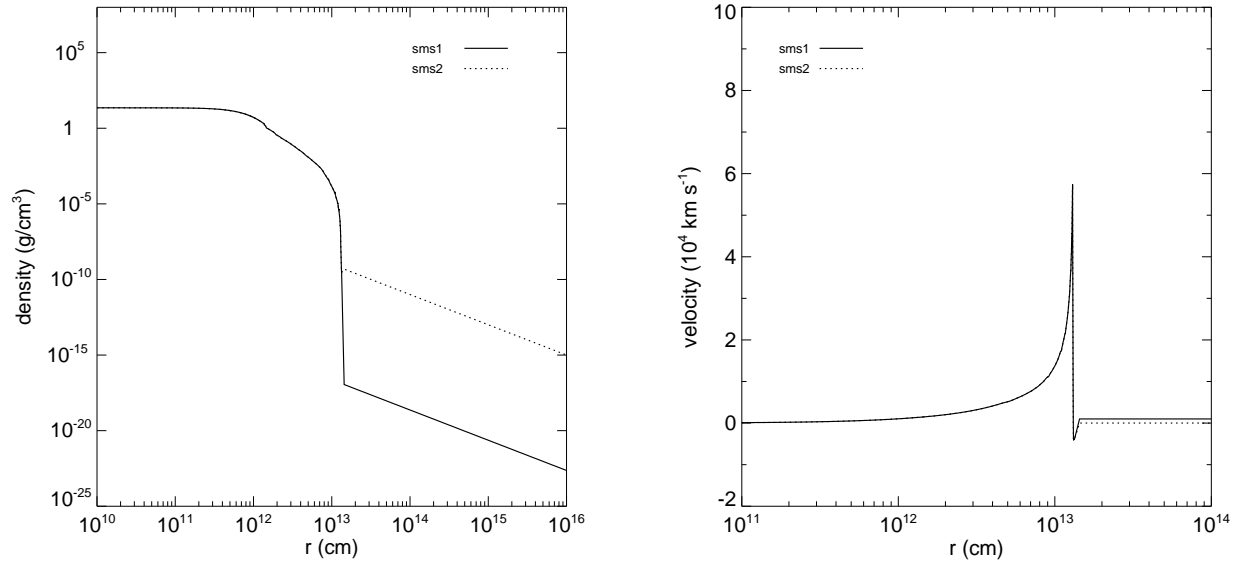

FIG. 3.— Initial RAGE explosion profiles. Right: densities. Left: velocities

also ensures that the photosphere of the shock is always resolved; failure to do so can lead to underestimates of luminosity during post processing. The radius of the shock in our setup is 1.3×10^{13} cm and our initial root grid has a resolution of 2.6×10^{9} cm with an outer boundary at 1.3×10^{14} cm.

We set reflecting and outflow boundary conditions on the fluid and radiation variables at the inner and outer boundaries of the grid, respectively. At the beginning of

the simulation, Courant times are short due to high temperatures, large velocities and small cell sizes. To minimize execution times and to accommodate the expansion of the SN, we periodically regrid the profiles onto a larger mesh as the explosion grows. Each time we regrid the SN we allocate 5000 zones out to either the edge of the shock (pre-breakout) or the edge of the radiation front (post-breakout). In the latter case we take the radius at which the radiation temperature falls to the wind temperature

(0.01 eV) to be the edge of the front. The inner boundary is always at the origin and the outer boundary of the final, largest mesh in our simulations is 1.0×10^{18} cm.

2.4. Circumstellar Envelope

We consider explosions in two kinds of envelope: low-mass outflows (SMS1) and massive inflows like those that grew the star to such large masses in such short times (SMS2). For diffuse outflows we adopt the usual power-law density profile for a wind at a constant velocity:

$$\rho_{\rm W}(r) = \frac{\dot{m}}{4\pi r^2 v_{\rm W}}. \tag{4}$$

Here, $\dot{m}$ is the mass loss rate associated with the wind and $v_{\rm W}$ is the wind speed. The mass loss rate is calculated from the total mass loss $M_{\rm tot}$ and the main sequence lifetime of the star $t_{\rm MSL}$:

$$\dot{m} = \frac{M_{\rm tot}}{t_{\rm MSL}}. \tag{5}$$

Since Pop III stars are not thought to lose much mass over their lives because there are no metals in their atmospheres to drive winds (Kudritzki 2000; Baraffe et al. 2001; Vink et al. 2001; Krtička & Kubát 2006), we set $M_{\rm tot} = 0.1\ M_{\odot}$ and $v_{\rm w} = 1000$ km s^{-1}.

We treat the massive infall envelope as a wind in reverse, with $\dot{m} = 0.01\ M_{\odot}$ yr^{-1} and an infall velocity $v_{\rm w} = 5$ km s^{-1}, in keeping with numerical simulations of baryon collapse in protogalaxies in strong LW backgrounds. This envelope assumes that accretion is spherical when in reality it may occur in a disk, so it should be considered to be the most massive one through which the SN shock might propagate. In both cases we take H and He mass fractions to be 76% and 24%, respectively, and for simplicity we take the wind to be cold ($T = 0.01$ eV) and neutral in all our models.

This latter assumption holds for dense envelopes, where semi-analytical studies have shown that ionizing UV photons cannot propagate more than a few dozen stellar radii from the star over its lifetime (Johnson et al. 2012b). On the other hand, the compact blue progenitor, with a total luminosity of 3.5×10^{42} erg s^{-1} and $T_{\rm eff} = 6.85 \times 10^4$ K, certainly ionizes the diffuse wind, so the light curves and spectra we calculate for that case should be taken as lower limits. We show initial RAGE density and velocity profiles for the shock, the star, and its surrounding envelope in Figure 3. The surface of the star is evident as the sharp drop in density at $\sim 1.4 \times 10^{13}$ cm. The fact that the infall density is more than seven orders of magnitude greater at the surface of the star than the outflow density has important consequences for shock and radiation breakout, as we discuss below. In both cases we evolve the SN out to 3 yr.

2.5. SPECTRUM

We calculate spectra for the explosions with the LANL SPECTRUM code. SPECTRUM directly sums the luminosity of every fluid element in a SN profile to calculate the total flux escaping the ejecta along the line of sight for 14900 wavelengths. The procedure is described in detail in Frey et al. (2012) and accounts for Doppler shifts and time dilation due to the relativistic expansion of the ejecta. SPECTRUM also calculates the intensities of emission lines and the attenuation of flux along the line of sight with OPLIB opacities, so it captures limb darkening and absorption lines imprinted on the flux by intervening material in the SN ejecta and envelope.

As explained in Frey et al. (2012), densities, velocities, radiation temperatures and mass fractions from the finest levels of refinement in the RAGE AMR hierarchy are extracted and ordered by radius into separate files, with one variable per file. These profiles usually contain more than 50,000 radial zones, so limits on machine memory and time prevent us from using all zones to calculate a spectrum. We therefore map only a subset of the points onto the new grid. We first sample the radiation energy density profile inward from the outer boundary to find the position of the radiation front, which we define to be where aT^4 rises above 1.0 erg/cm^3. This energy density is intermediate to that of the cold wind and the first photons to reach a given radius in the envelope. The radius of the $\tau = 20$ surface is then found by integrating the optical depth due to Thomson scattering inward from the outer boundary, where $\kappa_{Th} = 0.288$ gm^{-1} cm^2 for primordial H and He. This gives the greatest depth from which photons can escape from the ejecta because κ_{Th} is the minimum total opacity.

To compute a spectrum, we interpolate the densities, temperatures, velocities and mass fractions we extract from RAGE onto a 2D grid in r and $\mu = \cos\theta$ in SPECTRUM whose inner and outer boundaries are 0 and 10^{18} cm, respectively. The region from the center of the grid to the $\tau = 20$ surface is partitioned into one hundred uniform zones in log radius. We allocate 5000 uniform zones in radius between the $\tau = 20$ surface and the edge of the radiation front. The wind between the front and the outer boundary of the grid is divided into 100 uniform zones in log radius, for a total of 5200 radial bins. The fluid variables in each of these new radial bins is mass-averaged to ensure that SPECTRUM captures very sharp features in the original RAGE profile. The grid is discretized into 160 uniform zones in $\mu = \cos\theta$ from -1 to 1. Our choice of mesh yields good convergence in spectrum tests, fully resolving regions of the flow from which photons can escape the ejecta and only lightly sampling those from which they cannot.

3. BLAST PROFILES, LIGHT CURVES AND SPECTRA

We show velocity and gas temperature profiles at shock breakout for the SMS1 and SMS2 explosions in Figures 4 and 5. Before breakout, the SN cannot be seen by an external observer because photons from the shock are scattered by e$^-$ in the upper layers of the star. When the shock reaches the surface of the star it abruptly accelerates, as shown in the velocity profiles of Figures 4 and 5. The shock also releases a brief, intense pulse of photons into the envelope. This transient, which is mostly x-rays and hard UV, blows off the outer layers of the star, which detach from and accelerate ahead of the shock as we show at 8190 and 8540 s in the SMS1 velocities and at 8720 and 1.01e04 s in the SMS2 velocities. This effect is more pronounced in SMS1 because it is easier for the radiation front to drive a precursor into the diffuse wind than the dense infall. The advancing radiation front is visi-
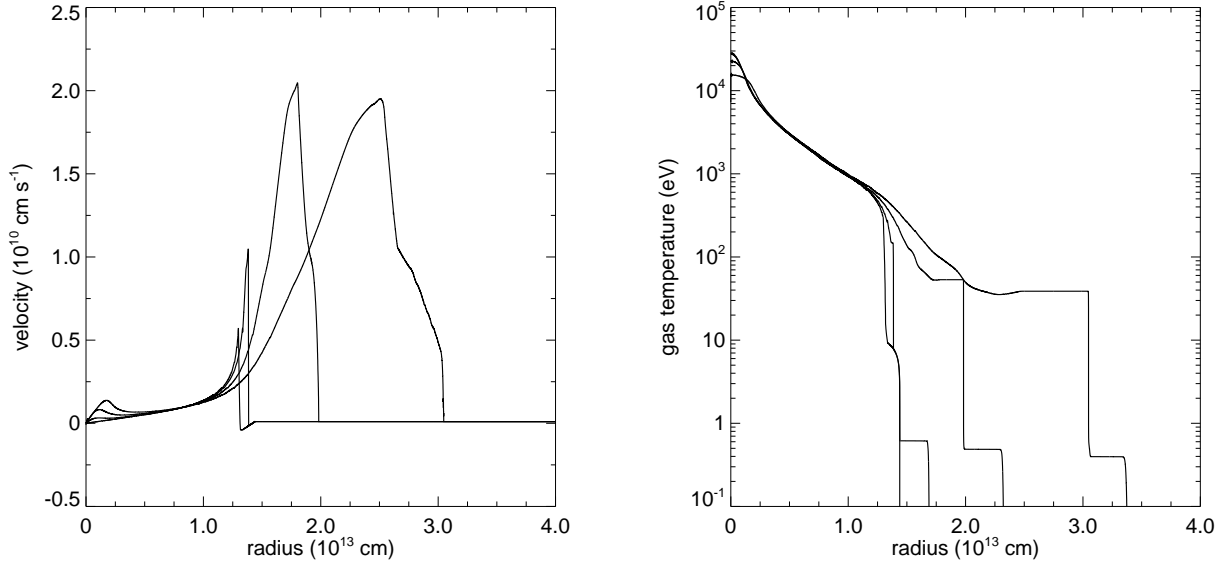
FIG. 4.— Shock breakout into a diffuse envelope (SMS1). Right: velocities; from left to right: 7980 s, 8050 s, 8190 s and 8540 s. Left: temperatures at the same times.
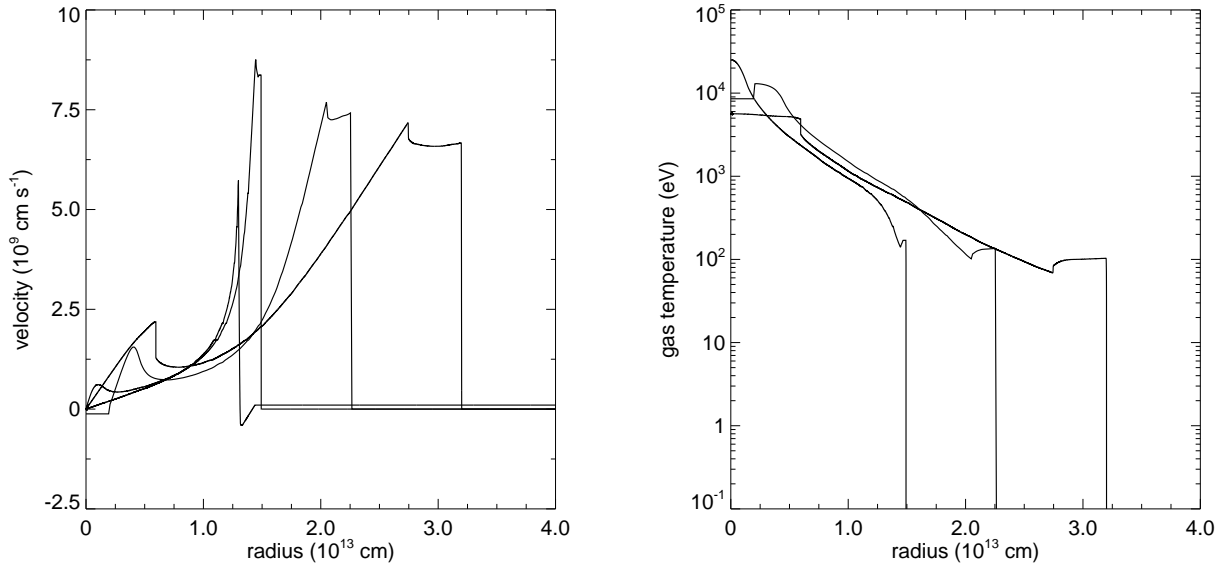

FIG. 5.— Shock breakout into dense infall (SMS2). Right: velocities; from left to right: 7980 s, 8100 s, 8720 s and 1.01e4 s. Left: temperatures at the same times.

ble as the flat plateau in gas temperature that extends from the outer edge of the shock into the surrounding medium. The temperature to which the radiation heats the gas falls as the shock expands, cools, and its spectrum softens (note that the temperature of the shock itself is much higher).

At breakout there are marked differences in the profiles of the two explosions as the shock plows into the envelope. First, in SMS1 the shock accelerates as it exits the star and then continues to speed up as it descends the density gradient of the diffuse wind. In SMS2 the shock accelerates but then slows down as it crashes out into the much denser infall envelope. The radiation front also advances more quickly into the diffuse wind than the infall. On the other hand, when the shock breaks out into the dense envelope it heats it to much higher temperatures. This hardens the spectrum of the shock and raises the

temperature of the surrounding gas to higher temperatures than in SMS1, ~ 100 eV instead of ~ 50 eV.

We show bolometric light curves for SMS1 and SMS2 in Figure 6. The light curve for SMS1 is similar to those of lower-mass Pop III PI SNe except that the explosion is approximately ten times as luminous, as shown by the overlaid u250 and z250 light curves from Whalen et al. (2012b). SMS1 exhibits the classic breakout transient, whose width is related to the light-crossing time of the star but is somewhat broader due to radiation-matter coupling effects as discussed in § 4.1 of Whalen et al. (2012b). Its light curve is similar in structure to that of z250, which is also the explosion of a compact blue giant (u250 is the PI SN of a 250 $M_\odot$ red hypergiant). The double peak at early times common to all 150 - 250 $M_\odot$ z-series PI SNe and the 55,500 $M_\odot$ PI SN is due to opacity effects. At breakout, the shock is extremely hot
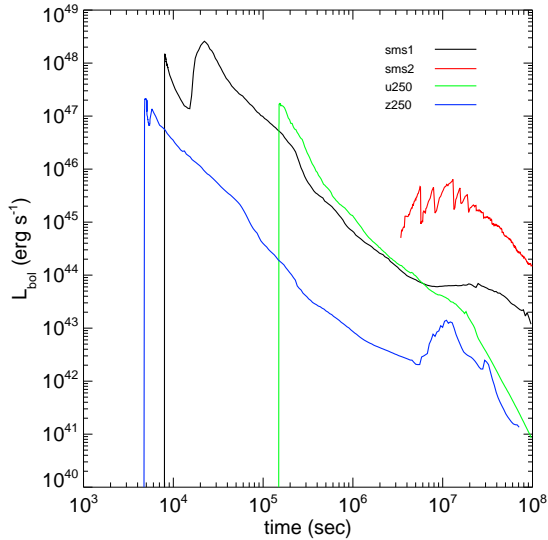
FIG. 6.— Bolometric luminosities for SMS1 and SMS2, together with light curves for the u250 and z250 PI SNe from Whalen et al. (2012b).
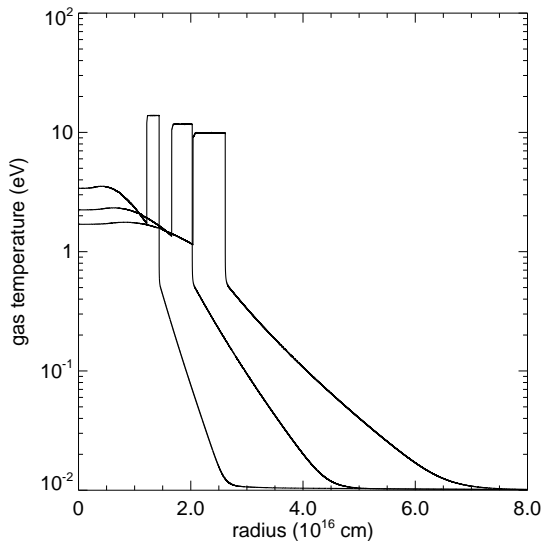

FIG. 7.— Radiation breakout in SMS2: gas temperatures at 3.69e6 s, 5.59e6 s, and 7.38e6 s.

and the thermal transient ionizes the envelope. Later, as the fireball expands it cools, and the opacity of the shock and the envelope fall and allow more photons to stream out into space. The double peak is absent in the u-series SNe because the shock is much cooler at breakout and never fully ionizes the envelope. At early times the luminosity of SMS1 comes from the conversion of kinetic energy into thermal energy by the shock. Later, its luminosity is due mostly to ejecta cooling, in contrast to low-mass PI SNe which are powered by ^{56}Ni decay. As in the z-series PI SNe, there is a resurgence in luminosity at $\sim 10^7$ s that is again due to opacity. At this time the $\tau = 1$ surface associated with the wavelength of peak emission in the spectrum has sunk to a hot layer deep in the ejecta, exposing it to the IGM and causing the SN to rebrighten.

Radiation breakout in SMS2 occurs far after shock breakout, at $\sim 5 \times 10^6$ s as we show in Figure 6. Radiation escapes the dense envelope much later because of its large optical depth, and when it happens it is gradual, as we show in Figure 7. Low-energy photons begin to leak out through the $\tau = 1$ surface for Thomson scattering at $\sim 2.5 \times 10^{16}$ cm by 3.7×10^6 s, and they are followed by more energetic photons by 5.6×10^6 s. At this point the shock is much cooler because of the large amount of PdV work it must perform on the dense shroud as it expands, but this results in an extremely luminous event in the NIR, as we discuss below.

After radiation breakout the shock appears to flicker until $\sim 2 \times 10^7$ s. This is due to radiative cooling and the cyclic formation and dissipation of a reverse shock in the ejecta. As the shock plows up the envelope a reverse shock breaks free from the forward shock and is driven into the interior of the ejecta in the frame of the flow. As the reverse shock detaches and recedes from the forward shock, it loses pressure support to radiative cooling by emission lines in the shocked gas and retreats back toward the forward shock. As the forward shock continues to sweep up the envelope a reverse shock again forms and backsteps from the forward shock. The cyclic heating and cooling of postshock gas associated with the oscillation of the reverse shock causes the fluctuations in luminosity from 5×10^6 - 2×10^7 s. The period of oscillation is determined by cooling rates in the gas (Chevalier & Imamura 1982; Imamura et al. 1984; Anninos et al. 1997) and is independent of the mass swept up by the ejecta. Such ripples are also found in Lyman alpha emission by primordial SN remnants as they sweep up neutral gas in cosmological halos on larger scales (note Figure 11 in Whalen et al. 2008). The light curves of both SMS1 and SMS2 are easily distinguished from those of less massive Pop III PI SNe.

We show velocity and density profiles for both explosions at intermediate to late times in Figures 8 and 9. Multiple reverse shocks reverberate through the interior of SMS1 at earlier times and mostly dissipate by 3 yr, although some structures are still visible in the velocity. These shocks are due to the internal dynamics of the ejecta rather than being driven inward by swept up gas (indeed, the remnant does not accumulate its own mass in ambient gas until it has grown to 6 pc). The density exhibits more self-similarity than the velocity, although its structure is always evolving in the vicinity of the shock from which most of the luminosity originates. The formation of a strong reverse shock due to plowed-up gas can be seen in the SMS2 velocity profiles from 10^5 s to 10^6 s, and it leads to multiple shocks at 10^7 s. This network of shocks is responsible for the oscillation in SMS2 bolometric luminosities from 10^6 - 2×10^7 s in Figure 6. The SMS2 density profiles are less self-similar over time, and there is significantly more evolution at the shock, as would be expected for ejecta plowing up a massive envelope.

4. NIR LIGHT CURVES

We calculate NIR light curves from our spectra with the photometry code developed by Su et al. (2011). Each spectrum is redshifted prior to removing the flux that is absorbed by intervening neutral hydrogen along the line of sight using the method of Madau (1995). The
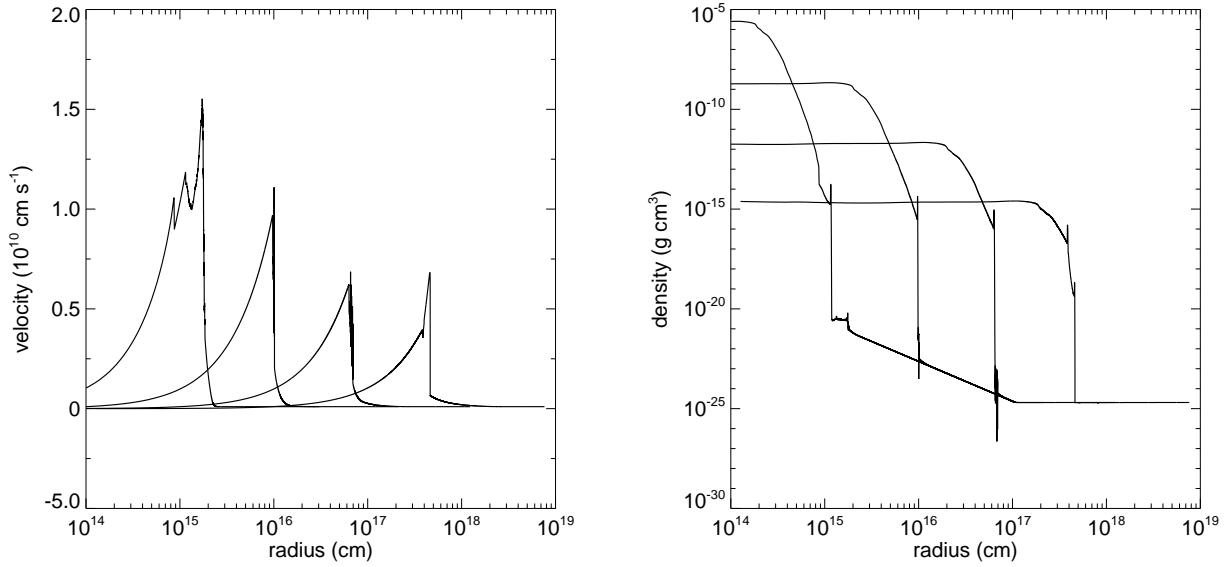
FIG. 8.— Evolution of SMS1 at intermediate and late times. Right: velocities; from left to right: 10^5 s, 10^6 s, 10^7 s and 10^8 s. Left: densities at the same times.
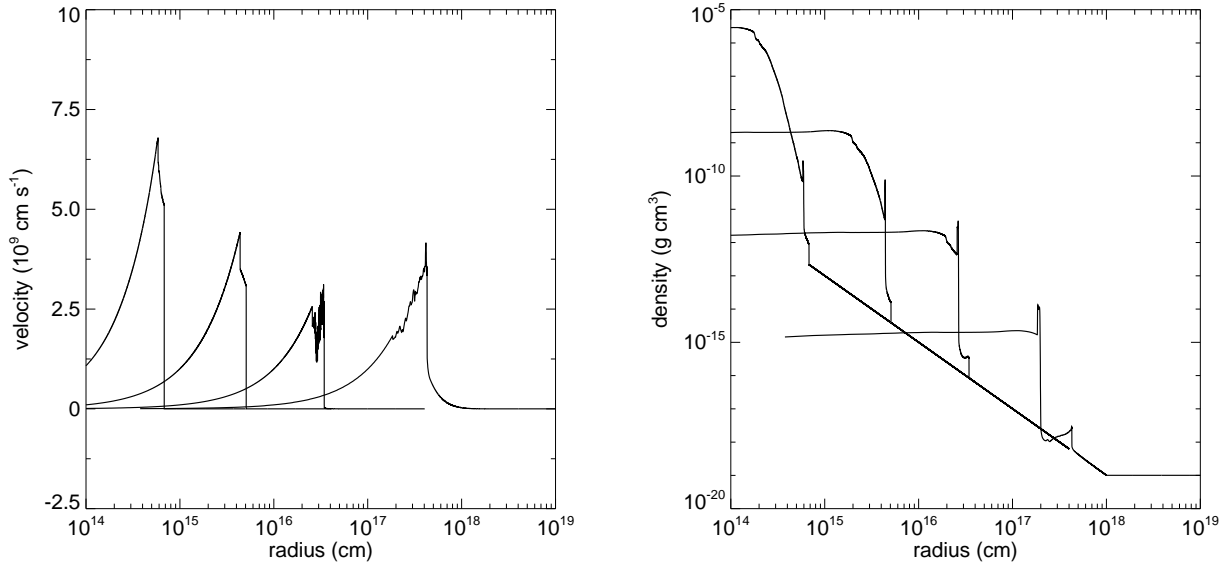

FIG. 9.— Evolution of SMS2 at intermediate and late times. Right: velocities; from left to right: 10^5 s, 10^6 s, 10^7 s and 10^8 s. Left: densities at the same times.

spectrum is then dimmed by the required cosmological factors for a specified redshift. The least sampled data is linearly interpolated between the input spectrum and filter curve to model the light curve in a given filter.

4.1. SMS1

NIR luminosities are plotted for SMS1 at $z = 7$, 10, 15, 20 and 30 in the left panel of Figure 10. The SN will be visible to *JWST* at all epochs for over 1000 days and can be detected by *WFIRST* out to $z \gtrsim 20$ for over 200 days. We include *JWST* for completeness, although given the much larger field of view of *WFIRST* and *WISH* and the low rates expected for this type of SN it is far more likely that such events will be detected in all-sky NIR surveys. SMS1 is extremely luminous in the NIR, with peak magnitudes ranging from 25 at $z = 7$ to 26.5 at $z = 20$. These light curves exhibit far more variability than

their redshifted bolometric light curves might suggest, eliminating any possibility that these events would be mistaken for high-redshift protogalaxies. This variation is due to the expansion and cooling of the fireball in the source frame.

The NIR profiles of SMS1 are easily distinguished from those of the u-series and z-series PI SNe in Whalen et al. (2012b) at all redshifts (see Figures 9 and 10). The SMS1 NIR light curves are similar in shape to those of z-series PI SNe, but z-series NIR luminosities never reach magnitudes brighter than 28 at $z > 7$. The SMS1 light curves evolve with redshift as expected: they broaden as z increases and the optimum filter wavelength increases with redshift. The NIR luminosities rise more quickly than they decline so these events are most easily detected in their early stages, but they nonetheless exhibit enough variability at any stage to be found in multiyear baseline

searches.

4.2. *SMS2*

We show NIR luminosities for SMS2 at $z = 7$, 10, 15, 20 and 30 in the right panel of Figure 10. They are quite different from those of SMS1. Consistent with radiation breakout from the shroud at ~ 58 days, no NIR signal is observed from these events until ~ 500 days at $z > 7$. This explosion eventually becomes hundreds of times brighter in the NIR than SMS1, with peak AB magnitudes from 21 at $z = 7$ to 23 at $z = 15$. It is visible to *JWST* for 200 days at all redshifts and for 200 days out to $z \gtrsim 20$ by *WFIRST* and *WISH*. The much higher NIR luminosities are due both to the large radius of the fireball at radiation breakout and the relatively low temperature of the shock at this radius (~ 10 eV) because of the PdV work the fireball must do against the dense envelope. These lower temperatures drive the redshifted peak of the shock's spectrum into the NIR in the source frame.

From $7 < z < 15$, the steady rise in luminosity from 500 - 700 days is due to the expansion of the surface area of the fireball, and the relative magnitudes of the three light curves are properly ordered in redshift. The shallow ripples in luminosity over these redshifts have much shorter periods than those in the bolometric luminosity in Figure 6 and are likely due to opacity fluctuations in the shock. The sudden drops in luminosity at 675 days and 700 days are due to sudden jumps in opacity that are associated with the cooling of the fireball. At $z > 15$, the SN is actually brighter in the *JWST* Mid-Infrared Instrument (MIRI) bands after 700 days than in the NIR, as we show in Figure 11.

In sum, SMS explosions in both diffuse winds and dense envelopes will be visible in *JWST* NIR deep fields out to $z \gtrsim 30$ and in all-sky NIR surveys by *WFIRST* and *WISH* out to $z \sim 20$, which is earlier than their likely era of formation. The fact that these NIR profiles change considerably with circumstellar envelope suggests that they will be powerful probes of the environments of such explosions. It is worth noting that even fully shrouded explosions will be visible at the earliest epochs. The envelopes we have chosen should bracket those in which SMS PI SNe will occur, so the NIR signals of actual explosions may be intermediate to those of these two events. As noted above, both SMS1 and SMS2 are easily distinguished from low-mass Pop III PI SNe as well as core-collapse SNe (Whalen et al. 2012d) and Type IIn SNe (Moriya et al. 2010; Whalen et al. 2012a).

5. CONCLUSION

The discovery of supermassive Pop III PI SNe would confirm for the first time that massive fragments capable of collapsing to $10^4 - 10^5$ $M_\odot$ SMBH seeds do form in primeval galaxies at high redshift. Although the rate of such events remains unknown, it might be thought that they are very rare because supermassive fragments must fall into a relatively narrow mass range to actually become stars and because few protogalaxies form in LW backgrounds capable of fully sterilizing them of H_2. However, recent developments suggest that these processes were more frequent than previously thought.

First, new simulations indicate that the assembly of protogalaxies in strong LW backgrounds may have been relatively common, yielding higher rates of SMBH seed production than might naively be inferred from the number density of $z \sim 7$ quasars, ~ 1 Gpc^{-3} (Agarwal et al. 2012). The sustained exponential growth required to reach such masses depended on the topology of cold flows over cosmic time (Di Matteo et al. 2012), so the scarcity of such flows may have governed the density of $z \sim 7$ quasars, not the rate of seed formation. Second, rotation could broaden the mass range over which supermassive stars encounter the pair instability by enhancing mixing and more rapidly building up massive He cores (Chatzopoulos & Wheeler 2012). Greater mass ranges imply larger event rates. Indeed, rotation, whose effects were not considered in the first studies of supermassive stellar evolution or in our simulations, may also increase the mass range over which supermassive fragments can actually become stars by supporting more of them against collapse and enabling stable nuclear burning.

A reasonable upper limit to SMS PI SN event rates are those of 140 - 260 $M_\odot$ Pop III PI SNe, which Whalen et al. (2012b) and others find to be $\sim 10^{-2}$ yr^{-1} deg^{-2} at $z \gtrsim 10$, which implies all-sky rates of up to $\sim 10^3$ yr^{-1} (Wise & Abel 2005; Weinmann & Lilly 2005; Tornatore et al. 2007; Trenti et al. 2009; Greif et al. 2010; Maio et al. 2011; Hummel et al. 2012; Johnson et al. 2012a; Wise et al. 2012). Although actual SMS PI SN event rates may be well below this limit, precluding their detection by *JWST*, they will clearly be bright enough to appear in wide field campaigns. They might also be detected in present NIR all-sky surveys by the *Subaru Hyper Suprime-Cam* at $z \gtrsim 3$ but further calculations will be necessary to confirm this (e.g., Tanaka et al. 2012; Moriya et al. 2012). Synchrotron emission from Pop III SNe at $z \gtrsim 10$ can be detected at 21 cm by existing observatories such as *eVLA* and *eMerlin* and future ones such as the *Square Kilometer Array* (*SKA*) (Meiksin & Whalen 2012). SMS PI SN explosions in dense envelopes may likewise generate enough synchrotron emission to be discovered in radio surveys.

Given that most supermassive stars will still directly collapse to BH, could there be other ways of detecting SMBH seed formation in protogalaxies? Past studies have shown that collapsing supermassive stars become extremely luminous in thermal neutrino emission as the central BH forms, with energies of ~ 10 MeV (Fuller et al. 1986; Shi et al. 1998). The prospects for detecting such neutrinos depends on the initial mass and entropy of the core. Although the total energy emitted from these massive stars increases linearly with mass, the entropy of their cores also increases with mass. Higher entropies lead to larger proto-black holes with lower peak densities and lower temperatures. Fryer & Heger (2011) found that the neutrino luminosity does not increase much with mass for stars above 10,000 $M_\odot$. The mean electron neutrino energy for stars above 10,000 $M_\odot$ is below 6 MeV and the μ_τ energy is not much higher. The collapse of such cores would be difficult to observe with neutrino detectors. However, if the core entropy is closer to that of a 1,000 $M_\odot$ star, the luminosity peaks more dramatically. Although even for these cores the mean electron neutrino energy is $\sim 7 - 8$ MeV, the μ_τ energy
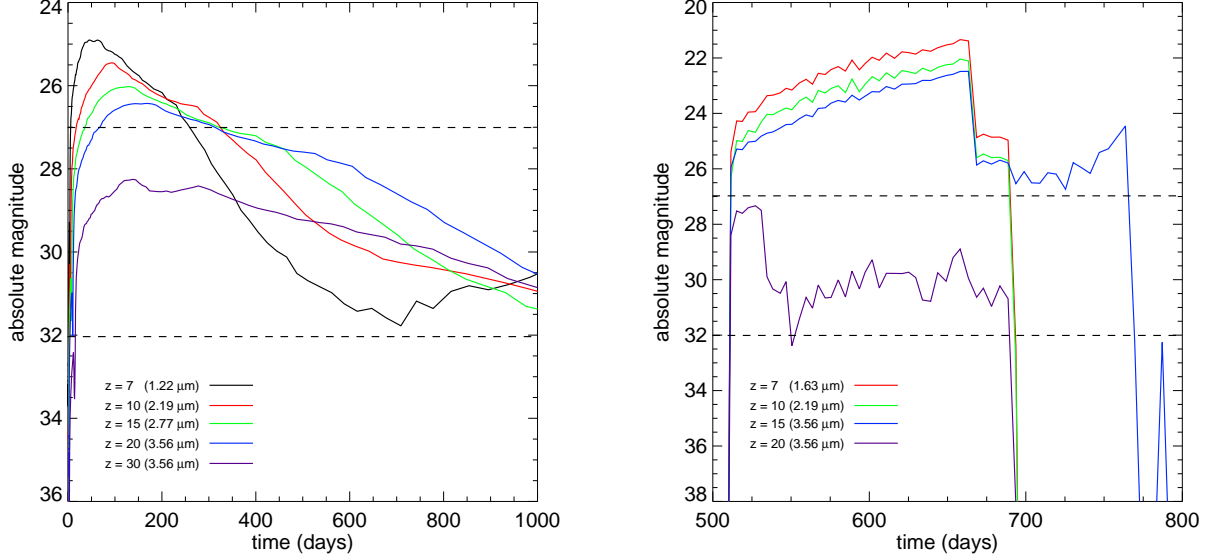
FIG. 10.— *JWST* NIRCam light curves for supermassive Pop III SNe in diffuse winds (SMS1, left panel) and dense envelopes (SMS2, right panel). The horizontal dashed lines at AB magnitudes 32 and 27 are the photometry limits for *JWST* and *WFIRST*, respectively.
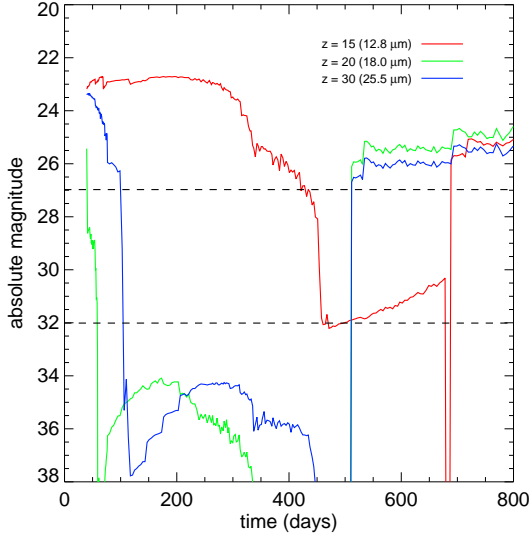

FIG. 11.— *JWST* MIRI NIR light curves for SMS2.

Surman et al. 2006, 2008). The nucleosynthetic signature of this process, which could be imprinted on stars that later form in the protogalaxy, depends on the temperature of the disk and hence the radius of the BH. It can therefore provide a diagnostic of the mass of the SMBH seed at birth, since massive BH with large event horizons burn at lower temperatures and yield chemical abundances that are distinct from those of smaller disks, which can burn all the way to Ni. Ancient, dim metal-poor stars bearing the ashes of this process could soon be discovered in ongoing surveys in the Galactic halo (e.g., Cayrel et al. 2004; Beers & Christlieb 2005; Frebel et al. 2005; Lai et al. 2008). The collapse of a supermassive star could also emit gravity waves (GWs) that might be detected in existing or future GW facilities (e.g., Fryer et al. 2002; Fryer & New 2011). These multi-messenger events, together with the most energetic supernovae in the universe, may soon herald the births of the first quasars.

lies in the 20-30 MeV range and would be more easily detected after cosmological redshifting. More detailed calculations are needed to be certain, but these cores would likely contribute to the neutrino background in detectors such as IceCube. If the density profile of the collapsing star also imposes a unique spectrum on the neutrino flux, it would facilitate its extraction from noise.

As noted in the Introduction, collapse may also lead to the formation of a black hole accretion disk system, with nuclear burning near the event horizon whose products could be expelled out into the halo by a jet (e.g.,

REFERENCES

Abel, T., Wise, J. H., & Bryan, G. L. 2007, ApJ, 659, L87
Agarwal, B., Khochfar, S., Johnson, J. L., Neistein, E., Dalla Vecchia, C., & Livio, M. 2012, ArXiv e-prints

Almgren, A. S., Beckner, V. E., Bell, J. B., Day, M. S., Howell, L. H., Joggerst, C. C., Lijewski, M. J., Nonaka, A., Singer, M., & Zingale, M. 2010, ApJ, 715, 1221

Alvarez, M. A., Bromm, V., & Shapiro, P. R. 2006, ApJ, 639, 621

Anninos, P., Zhang, Y., Abel, T., & Norman, M. L. 1997, New Astronomy, 2, 209

Baraffe, I., Heger, A., & Woosley, S. E. 2001, ApJ, 550, 890

Barkat, Z., Rakavy, G., & Sack, N. 1967, Physical Review Letters, 18, 379

Beers, T. C. & Christlieb, N. 2005, ARA&A, 43, 531

Begelman, M. C. 2010, MNRAS, 402, 673

Begelman, M. C., Rossi, E. M., & Armitage, P. J. 2008, MNRAS, 387, 1649

Begelman, M. C., Volonteri, M., & Rees, M. J. 2006, MNRAS, 370, 289

Cayrel, R., Depagne, E., Spite, M., Hill, V., Spite, F., François, P., Plez, B., Beers, T., Primas, F., Andersen, J., Barbuy, B., Bonifacio, P., Molaro, P., & Nordström, B. 2004, A&A, 416, 1117

Chatzopoulos, E. & Wheeler, J. C. 2012, ApJ, 748, 42

Chen, K.-J., Heger, A., & Almgren, A. S. 2011, Computer Physics Communications, 182, 254

Chevalier, R. A. & Imamura, J. N. 1982, ApJ, 261, 543

Di Matteo, T., Khandai, N., DeGraf, C., Feng, Y., Croft, R. A. C., Lopez, J., & Springel, V. 2012, ApJ, 745, L29

Frebel, A., Aoki, W., Christlieb, N., Ando, H., Asplund, M., Barklem, P. S., Beers, T. C., Eriksson, K., Fechner, C., Fujimoto, M. Y., Honda, S., Kajino, T., Minezaki, T., Nomoto, K., Norris, J. E., Ryan, S. G., Takada-Hidai, M., Tsangarides, S., & Yoshii, Y. 2005, Nature, 434, 871

Frey, L. H., Even, W., Whalen, D. J., Fryer, C. L., Hungerford, A. L., Fontes, C. J., & Colgan, J. 2012, arXiv:1203.5832

Fryer, C. L. & Heger, A. 2011, Astronomische Nachrichten, 332, 408

Fryer, C. L., Holz, D. E., & Hughes, S. A. 2002, ApJ, 565, 430

Fryer, C. L. & New, K. C. B. 2011, Living Reviews in Relativity, 14, 1

Fuller, G. M., Woosley, S. E., & Weaver, T. A. 1986, ApJ, 307, 675

Gal-Yam, A., Mazzali, P., Ofek, E. O., Nugent, P. E., Kulkarni, S. R., Kasliwal, M. M., Quimby, R. M., Filippenko, A. V., Cenko, S. B., Chornock, R., Waldman, R., Kasen, D., Sullivan, M., Beshore, E. C., Drake, A. J., Thomas, R. C., Bloom, J. S., Poznanski, D., Miller, A. A., Foley, R. J., Silverman, J. M., Arcavi, I., Ellis, R. S., & Deng, J. 2009, Nature, 462, 624

Gardner, J. P., Mather, J. C., Clampin, M., Doyon, R., Greenhouse, M. A., Hammel, H. B., Hutchings, J. B., Jakobsen, P., Lilly, S. J., Long, K. S., Lunine, J. I., McCaughrean, M. J., Mountain, M., Nella, J., Rieke, G. H., Rieke, M. J., Rix, H.-W., Smith, E. P., Sonneborn, G., Stiavelli, M., Stockman, H. S., Windhorst, R. A., & Wright, G. S. 2006, Space Sci. Rev., 123, 485

Gittings, M., Weaver, R., Clover, M., Betlach, T., Byrne, N., Coker, R., Dendy, E., Hueckstaedt, R., New, K., Oakes, W. R., Ranta, D., & Stefan, R. 2008, Computational Science and Discovery, 1, 015005

Greif, T. H., Glover, S. C. O., Bromm, V., & Klessen, R. S. 2010, ApJ, 716, 510

Heger, A. & Woosley, S. E. 2002, ApJ, 567, 532

—. 2010, ApJ, 724, 341

Hummel, J. A., Pawlik, A. H., Milosavljević, M., & Bromm, V. 2012, ApJ, 755, 72

Imamura, J. N., Wolff, M. T., & Durisen, R. H. 1984, ApJ, 276, 667

Inayoshi, K. & Omukai, K. 2012, MNRAS, 422, 2539

Joggerst, C. C., Almgren, A., Bell, J., Heger, A., Whalen, D., & Woosley, S. E. 2010, ApJ, 709, 11

Joggerst, C. C. & Whalen, D. J. 2011, ApJ, 728, 129

Johnson, J. L., Dalla Vecchia, C., & Khochfar, S. 2012a, arXiv:1206.5824

Johnson, J. L., Whalen, D. J., Fryer, C. L., & Li, H. 2012b, ApJ, 750, 66

Kasen, D., Woosley, S. E., & Heger, A. 2011, ApJ, 734, 102

Kitayama, T., Yoshida, N., Susa, H., & Umemura, M. 2004, ApJ, 613, 631

Krtička, J. & Kubát, J. 2006, A&A, 446, 1039

Kudritzki, R. 2000, in The First Stars, ed. A. Weiss, T. G. Abel, & V. Hill, 127–+

Lai, D. K., Bolte, M., Johnson, J. A., Lucatello, S., Heger, A., & Woosley, S. E. 2008, ApJ, 681, 1524

Madau, P. 1995, ApJ, 441, 18

Magee, N. H., Abdallah, Jr., J., Clark, R. E. H., Cohen, J. S., Collins, L. A., Csanak, G., Fontes, C. J., Gauger, A., Keady, J. J., Kilcrease, D. P., & Merts, A. L. 1995, in Astronomical Society of the Pacific Conference Series, Vol. 78, Astrophysical Applications of Powerful New Databases, ed. S. J. Adelman & W. L. Wiese, 51

Maio, U., Khochfar, S., Johnson, J. L., & Ciardi, B. 2011, MNRAS, 414, 1145

Meiksin, A. & Whalen, D. J. 2012, arXiv:1209.1915

Moriya, T., Yoshida, N., Tominaga, N., Blinnikov, S. I., Maeda, K., Tanaka, M., & Nomoto, K. 2010, in American Institute of Physics Conference Series, Vol. 1294, American Institute of Physics Conference Series, ed. D. J. Whalen, V. Bromm, & N. Yoshida, 268–269

Moriya, T. J., Blinnikov, S. I., Tominaga, N., Yoshida, N., Tanaka, M., Maeda, K., & Nomoto, K. 2012, arXiv:1204.6109

Mortlock, D. J., Warren, S. J., Venemans, B. P., Patel, M., Hewett, P. C., McMahon, R. G., Simpson, C., Theuns, T., Gonzáles-Solares, E. A., Adamson, A., Dye, S., Hambly, N. C., Hirst, P., Irwin, M. J., Kuiper, E., Lawrence, A., & Röttgering, H. J. A. 2011, Nature, 474, 616

Ohkubo, T., Nomoto, K., Umeda, H., Yoshida, N., & Tsuruta, S. 2009, ApJ, 706, 1184

Pan, T., Kasen, D., & Loeb, A. 2012a, MNRAS, 422, 2701

Pan, T., Loeb, A., & Kasen, D. 2012b, MNRAS, 423, 2203

Rakavy, G. & Shaviv, G. 1967, ApJ, 148, 803

Regan, J. A. & Haehnelt, M. G. 2009, MNRAS, 396, 343

Scannapieco, E., Madau, P., Woosley, S., Heger, A., & Ferrara, A. 2005, ApJ, 633, 1031

Sethi, S., Haiman, Z., & Pandey, K. 2010, ApJ, 721, 615

Shang, C., Bryan, G. L., & Haiman, Z. 2010, MNRAS, 402, 1249

Shi, X., Fuller, G. M., & Halzen, F. 1998, Physical Review Letters, 81, 5722

Su, J., Stiavelli, M., Oesch, P., Trenti, M., Bergeron, E., Bradley, L., Carollo, M., Dahlen, T., Ferguson, H. C., Giavalisco, M., Koekemoer, A., Lilly, S., Lucas, R. A., Mobasher, B., Panagia, N., & Pavlovsky, C. 2011, ApJ, 738, 123

Surman, R., McLaughlin, G. C., & Hix, W. R. 2006, ApJ, 643, 1057

Surman, R., McLaughlin, G. C., Ruffert, M., Janka, H.-T., & Hix, W. R. 2008, ApJ, 679, L117

Tanaka, M., Moriya, T. J., Yoshida, N., & Nomoto, K. 2012, MNRAS, 422, 2675

Tornatore, L., Ferrara, A., & Schneider, R. 2007, MNRAS, 382, 945

Trenti, M., Stiavelli, M., & Michael Shull, J. 2009, ApJ, 700, 1672

Vink, J. S., de Koter, A., & Lamers, H. J. G. L. M. 2001, A&A, 369, 574

Volonteri, M. & Begelman, M. C. 2010, MNRAS, 409, 1022

Weaver, T. A., Zimmerman, G. B., & Woosley, S. E. 1978, ApJ, 225, 1021

Weinmann, S. M. & Lilly, S. J. 2005, ApJ, 624, 526

Whalen, D., Abel, T., & Norman, M. L. 2004, ApJ, 610, 14

Whalen, D., van Veelen, B., O'Shea, B. W., & Norman, M. L. 2008, ApJ, 682, 49

Whalen, D. J., Even, W., Lovekin, C. C., Fryer, C. L., Holz, D. H., Stiavelli, M., & Knight, C. 2012a, ApJ, submitted

Whalen, D. J., Frey, L. H., Even, W., Fryer, C. L., Holz, D. H., Stiavelli, M., Heger, A. H., Hungerford, A. L., & Lovekin, C. C. 2012b, ApJ, submitted

Whalen, D. J., Fryer, C. L., Holz, D. E., Heger, A., Woosley, S. E., Stiavelli, M., Even, W., & Frey, L. L. 2012c, arXiv:1209.3457

Whalen, D. J., Joggerst, C. C., Fryer, C. L., Stiavelli, M., Heger, A., & Holz, D. E. 2012d, arXiv:1209.5459

Whalen, D. J., Xu, H., Johnson, J. L., Li, H., & Fryer, C. L. 2012e, ApJ, in prep

Wise, J. H. & Abel, T. 2005, ApJ, 629, 615

—. 2008, ApJ, 684, 1

Wise, J. H., Turk, M. J., & Abel, T. 2008, ApJ, 682, 745

Wise, J. H., Turk, M. J., Norman, M. L., & Abel, T. 2012, ApJ, 745, 50

Wolcott-Green, J., Haiman, Z., & Bryan, G. L. 2011, MNRAS, 418, 838

Woosley, S. E., Heger, A., & Weaver, T. A. 2002, Reviews of Modern Physics, 74, 1015